ICAS 2021 SHANG HAI
International Council of the Aeronautical Sciences
32nd Congress of the International Council of the Aeronautical Sciences
September 6-10, 2021
Pudong Shangri-La, Shanghai, China

A CONTRIBUTION TO THE SIMULATION OF TRANSITIONAL FLOWS OVER AEROSPACE CONFIGURATIONS

Leonardo Motta Maia de Oliveira Carvalho[1], Ricardo Galdino da Silva[2] & João Luiz F. Azevedo[2]

[1]Instituto Tecnológico de Aeronáutica, 12228-900 São José dos Campos, SP, Brazil
[2]Instituto de Aeronáutica e Espaço, 12228-904 São José dos Campos, SP, Brazil

Abstract

The study of transitional flows over aerospace configurations is the main concern of the present work. The present effort is conducted using an in-house developed Computational Fluid Dynamics (CFD) code which uses a correlation-based transition model in order to include transition prediction capabilities into the theoretical formulation. The code solves the Reynolds-averaged Navier-Stokes (RANS) equations using an upwind spatial discretization approach and a point implicit time marching algorithm. Three aerospace relevant test cases are selected. These cases are addressed due to their dependency on transition phenomena in order to adequately describe the resulting flowfield and their strong relationship with aerospace applications.

Keywords: Laminar-turbulent transition; Aerospace applications; CFD; Transition modeling

1. Introduction

The comparison of laminar and turbulent flows indicates that the smooth alignment of the streamlines inside laminar boundary layers generates less skin friction and heat transfer than turbulent boundary layers. However, the thicker turbulent boundary layers are less prone to separation when subjected to strong adverse pressure gradients[1]. The differences associated with laminar and turbulent flows imply that, for a given aerospace vehicle, laminar or turbulent boundary layers can present advantages and disadvantages depending on the operational condition. Hence, it is important that the transition process can be adequately understood in order to develop more efficient aerospace vehicles.

Although high fidelity tools, such as Direct Numerical Simulations (DNS), are available to accurately predict transition at any condition, their computational costs are still prohibitive for applications to realistic flight configurations. Due to this prohibitive high computational cost, simpler methodologies are used, such as empirical correlations and linear e^n methods [1, 2]. However, their simplicity implies that a large amount of assumptions are needed in order to construct their theoretical basis. This realization, on the other hand, means that the application of such methodologies to complex configurations is not straightforward. Moreover, most of these less demanding techniques are dependent on non-local variables, making their integration into modern parallel unstructured Computational Fluid Dynamics (CFD) codes difficult from a computational standpoint [3, 4].

An organic way to include transition modeling capabilities in modern CFD codes, without complex and expensive algorithms, would be to modify currently available turbulent closures. These well established closures are mostly based on local variables and have been extensively tested on modern CFD codes. This approach to predict transition is actually used in the $\gamma - Re_\theta$ [1, 2] transition model which is coupled to the SST closure [5]. This transition model solves two transport equations, one for the intermittency and another for the momentum thickness Reynolds number, in order to predict transition. These transport equations are, then, combined with the source terms of the SST closure in order to trigger the production of eddy-viscosity, μ_t, in key places where the flow would be, indeed, in a turbulent state. This approach is used in the present work and the transition model is implemented into an existing, in-house developed, CFD code [6, 7]. As the results included in the paper demonstrate, the addition of transition modeling has improved the correlation with experimental data.

2. Theoretical Formulation

In order to study transitional flows, the Reynolds-averaged Navier-Stokes (RANS) equations are solved together with an appropriate turbulence closure and a transition model in a strongly coupled fashion [6, 7, 8]. This section discusses the relevant issues associated with the theoretical formulation.

2.1 Reynolds-Averaged Navier-Stokes Equations

The RANS equations can be written in Cartesian coordinates as

$$\frac{\partial \mathbf{Q}}{\partial t} + \nabla \cdot (\mathbf{E}_e - \mathbf{E}_v) = 0 \, . \tag{1}$$

Here, $\mathbf{Q}$ is the vector of conserved properties, and $\mathbf{E}_e$ and $\mathbf{E}_v$ are the inviscid and viscous flux vectors, respectively. These algebraic vectors can be written as

$$\mathbf{Q} = \begin{Bmatrix} \rho \\ \rho u \\ \rho v \\ \rho w \\ e \end{Bmatrix} \, , \qquad \mathbf{E}_e = \begin{Bmatrix} \rho \mathbf{v} \\ \rho u \mathbf{v} + p\hat{i}_x \\ \rho v \mathbf{v} + p\hat{i}_y \\ \rho w \mathbf{v} + p\hat{i}_z \\ (e+p)\mathbf{v} \end{Bmatrix} \, , \qquad \mathbf{E}_v = \begin{Bmatrix} 0 \\ \left(\tau^{\ell}_{xj} + \tau^{t}_{xj}\right)\hat{i}_j \\ \left(\tau^{\ell}_{yj} + \tau^{t}_{yj}\right)\hat{i}_j \\ \left(\tau^{\ell}_{zj} + \tau^{t}_{zj}\right)\hat{i}_j \\ \beta_j \hat{i}_j \end{Bmatrix} \, . \tag{2}$$

The viscous stress tensor is defined as

$$\tau^{\ell}_{ij} = \mu_{\ell} \left[\left(\frac{\partial u_i}{\partial x_j} + \frac{\partial u_j}{\partial x_i} \right) - \frac{2}{3} \left(\frac{\partial u_m}{\partial x_m} \right) \delta_{ij} \right] \, , \tag{3}$$

and the components of the heat conduction vector can be written as

$$q_j = -\gamma \left(\frac{\mu_{\ell}}{Pr} + \frac{\mu_t}{Pr_t} \right) \frac{\partial (e_i)}{\partial x_j} \, . \tag{4}$$

In the previous equations, $\mathbf{v}$ is the velocity vector and τ^{t}_{ij} are the components of the turbulent stress tensor, which, for the closure considered in the present work, have an expression similar to that shown in Eq. (3), except that the eddy-viscosity coefficient, μ_t, replaces the laminar dynamic viscosity coefficient, μ_{ℓ}.

2.2 Turbulence Closure

The $\gamma - Re_{\theta}$ transition model is coupled with the SST turbulence closure [5] in order to model the transition effects in the field. In this context, the transition formulation limits the production and destruction of turbulent kinetic energy, k. The SST turbulence closure equations can be written as

$$\begin{aligned} \frac{\partial (\rho k)}{\partial t} + \frac{\partial (\rho u_j k)}{\partial x_j} &= P_k - \beta^* \rho \omega k + \frac{\partial}{\partial x_j} \left[(\mu + \sigma_k \mu_t) \frac{\partial k}{\partial x_j} \right] \, , \\ \frac{\partial (\rho \omega)}{\partial t} + \frac{\partial (\rho u_j \omega)}{\partial x_j} &= \frac{\gamma}{\nu_t} P_k - \beta \rho \omega^2 + \frac{\partial}{\partial x_j} \left[(\mu + \sigma_{\omega} \mu_t) \frac{\partial \omega}{\partial x_j} \right] + 2(1 - F_1) \frac{\rho \sigma_{\omega 2}}{\omega} \frac{\partial k}{\partial x_j} \frac{\partial \omega}{\partial x_j} \, . \end{aligned} \tag{5}$$

In the above equations, P_k stands for the production term,

$$P_k = \tau_{ij} \frac{\partial u_i}{\partial x_j} \, , \tag{6}$$

τ_{ij} is the shear-stress tensor,

$$\tau_{ij} = \mu_t \left(2 S_{ij} - \frac{2}{3} \frac{\partial u_k}{\partial x_k} \delta_{ij} \right) - \frac{2}{3} \rho k \delta_{ij} \, , \tag{7}$$

and S_{ij} is the compressible strain rate, defined as

$$S_{ij} = \frac{1}{2}\left(\frac{\partial u_i}{\partial x_j} + \frac{\partial u_j}{\partial x_i}\right) . \tag{8}$$

Since the original SST closure combines the high Reynolds number Wilcox $k-\omega$ model [9] with the standard $k-\varepsilon$ closure [10], a blending function is used to gradually switch between both model constants, as defined in Ref. [11], and it can be written as

$$\phi = F_1\phi_1 + (1-F_1)\phi_2 . \tag{9}$$

In this expression, ϕ_1 is an arbitrary constant of the $k-\omega$ closure and ϕ_2 is the corresponding constant of the $k-\varepsilon$ model. Moreover, the definitions needed to build the blending function, F_1, are:

$$F_1 = \tanh\left(\arg_1^4\right) , \tag{10}$$

$$\arg_1 = \min\left[\max\left(\frac{\sqrt{k}}{\beta^*\omega d}, \frac{500\nu}{d^2\omega}\right), \frac{4\rho\sigma_{\omega 2}k}{\mathrm{CD}_{k\omega}d^2}\right], \tag{11}$$

$$\mathrm{CD}_{k\omega} = \max\left(2\rho\sigma_{\omega 2}\frac{1}{\omega}\frac{\partial k}{\partial x_j}\frac{\partial \omega}{\partial x_j}, 10^{-20}\right), \tag{12}$$

$$F_2 = \tanh\left(\arg_2^2\right), \tag{13}$$

$$\arg_2 = \max\left(2\frac{\sqrt{k}}{\beta^*\omega d}, \frac{500\nu}{d^2\omega}\right). \tag{14}$$

The differences between the implemented version of the model and the original definition, proposed in Ref. [5], are focused on the eddy-viscosity coefficient definition, production limiter for turbulent kinetic energy and two of the model constants. Moreover, the eddy-viscosity coefficient definition in the SST closure proposed in Ref. [11] can be written as

$$\mu_t = \frac{\rho a_1 k}{\max(a_1\omega, SF_2)}, \qquad S = \sqrt{2S_{ij}S_{ij}}. \tag{15}$$

The production limiter of turbulent kinetic energy, k, is defined as

$$P_k = \min(P_k, 10\beta^*\rho\omega k). \tag{16}$$

The two constants modified in the updated version of the SST closure, γ_1 and γ_2, have their values re-defined as

$$\gamma_1 = 5/9; \qquad \gamma_2 = 0.44. \tag{17}$$

The other terms in Eq. (5), that are not explained in this section, are equivalent between both versions of the SST closure and they can be found in Refs. [5, 11].

2.3 Transition Modeling

The transition model formulation used is based on the $\gamma - Re_\theta$ approach proposed in Refs. [4, 12]. The approach solves two transport equations in order to account for transitional behavior of the flowfield. These equations can be written as:

$$\begin{aligned} \frac{\partial(\rho\gamma)}{\partial t} + \frac{\partial(\rho u_j\gamma)}{\partial x_j} &= P_\gamma - E_\gamma + \frac{\partial}{\partial x_j}\left[\left(\mu + \frac{\mu_t}{\sigma_f}\right)\frac{\partial\gamma}{\partial x_j}\right] \\ \frac{\partial(\rho\hat{R}e_{\theta t})}{\partial t} + \frac{\partial(\rho u_j\hat{R}e_{\theta t})}{\partial x_j} &= P_{\theta t} + \frac{\partial}{\partial x_j}\left[\sigma_{\theta t}(\mu+\mu_t)\frac{\partial\hat{R}e_{\theta t}}{\partial x_j}\right] . \end{aligned} \tag{18}$$

In this formulation, γ is the intermittency, which assumes the value of 1 for turbulent regions and 0 for laminar regions, and $\hat{R}e_\theta$ is the transition momentum thickness Reynolds number, which triggers the production term of γ. The complete formulation of the transition model used can be seen in Refs. [4, 12, 13]

3. Numerical Formulation

3.1 Finite Volume Discretization

The RANS and turbulence model equations are discretized using a cell-centered finite volume method [14]. The spatially discretized equations can be written as

$$\frac{\partial \mathbf{Q}_i}{\partial t} = -\frac{1}{V_i}\sum_{k=1}^{n_f}\left[\left(\mathbf{E}_{e_k} - \mathbf{E}_{v_k}\right)\cdot \mathbf{S}_k\right] . \tag{19}$$

Here, k indicates the number of the face, n_f is the total number of faces of the i-th control volume, and $\mathbf{S}_k$ is the area of the k-th face. For the convective flux computations, in order to include appropriate numerical dissipation, the Roe flux-difference splitting scheme [15] is used. Hence, the inviscid flux contribution for the k-th face can be written as

$$\mathbf{E}_{e_k}\cdot\mathbf{S}_k = \mathbf{E}_e\left(\mathbf{Q}_k\right)\cdot\mathbf{S}_k - \frac{1}{2}\left|\tilde{\mathbf{A}}_k\right|\left|\mathbf{S}_k\right|\left(\mathbf{Q}_R - \mathbf{Q}_L\right) , \tag{20}$$

where $\mathbf{Q}_k = 0.5\left(\mathbf{Q}_R + \mathbf{Q}_L\right)$ and $\left|\tilde{\mathbf{A}}_k\right|$ is the Roe matrix, formed with the magnitude of the eigenvalues associated with the k-th face normal direction.

In cell-centered schemes, viscous fluxes are typically constructed by computing cell-averaged derivatives in each control volume and, then, extrapolating these derivative to cell interfaces or cell faces. These two procedures combined can greatly influence the numerical robustness of CFD tools as discussed in Refs. [16, 17] and, in the specific case of the present solver, in Ref. [18]. Here, the approach that has demonstrated to be the most robust one, among those tested in Ref. [18], is adopted. This approach computes the cell-averaged derivatives using the Green-Gauss theorem, which can be defined as

$$\left(\frac{\partial\phi}{\partial x}\right)_i = \frac{1}{V_i}\int_{V_i}\frac{\partial\phi}{\partial x}dV = \frac{1}{V_i}\int_{s_i}\phi\hat{n}_x\cdot dS . \tag{21}$$

Here, ϕ is the property of an arbitrary control volume, i, $\hat{n}_x$ represents the component in the x direction of the outward unit normal vector, V_i and S_i are the i-th cell volume and external face area. The derivative values are, then, extrapolated to the cell interfaces using a volume weighted procedure, which is defined as

$$\left(\frac{\partial\phi}{\partial x}\right)_f = \frac{1}{V_i + V_j}\left(V_i\nabla\phi_i + V_j\nabla\phi_j\right)\cdot\hat{n}_x . \tag{22}$$

Following the cell-averaged derivative definition, ϕ is an arbitrary property and the f, i and j subscripts are denoting, respectively, the interface index, the cell to the left and the cell to the right of the interface. As before, $\hat{n}_x$ is the component in the x direction of the outward unit normal vector with respect to the i-th cell.

3.2 Time Integration

An implicit time-stepping scheme based on the symmetric Gauss-Seidel method is used in order to advance the solution in time. The implicit scheme used here is detailed in Ref. [7]. Its general form, including boundary conditions, can be expressed as

$$\left[\frac{V_i}{\Delta t_i}\mathbf{I} + \sum_{k=1}^{n_f}\frac{\partial\left(\mathbf{E}_k\cdot\mathbf{S}_k\right)}{\partial\mathbf{Q}_i} + \sum_{K_{BC}}\frac{\partial\left(\mathbf{E}_k\cdot S_k\right)}{\partial\mathbf{Q}_{nb}}\mathbf{B}_{nb}\right]\Delta\mathbf{Q}_i = -\sum_{k=1}^{n_f}\mathbf{E}_k\cdot\mathbf{S}_k - \sum_{k_{int}}\frac{\partial\left(\mathbf{E}_k\cdot\mathbf{S}_k\right)}{\partial\mathbf{Q}_{nb}}\Delta\mathbf{Q}_{nb} . \tag{23}$$

More information about the time integration procedures that are being used in the present solver can be found in Refs. [8, 7].

4. Numerical Results and Discussion

4.1 *Aerospatiale-A* Airfoil

The *Aerospatiale-A* is characterized by a fairly large thickness to chord ratio. This expressive thickness imposes large adverse pressure gradients over the boundary layer at high angles-of-attack. These conditions, at lower Reynolds numbers, usually cause a laminar separation bubble over the

upper surface of the airfoil. For the *Aerospatiale-A*, the laminar separation bubble (LSB) occurs at $x/c = 0.12$ and re-attaches at $x/c = 0.83$ and it is ignored if the flow is considered fully turbulent. Therefore, this case is a very good application for transition modeling.

The flow over the *Aerospatiale-A* airfoil was also used as a test case in Ref. [12], which is one of the original references associated with the $\gamma - Re_\theta$ transition model. In the context of the present research group, this test case has also been used in a similar study using a commercial CFD solver [2, 19]. In any event, the test case makes for a good reference verification case as plenty of comparison data is readily available. However, it should be noted that these reference numerical results were generated using different meshes from the one in use in the present effort. The flight conditions considered in order to study the subsonic flow around this airfoil are freestream Mach number $M_\infty = 0.15$, angle of attack $\alpha = 13.3$ deg., reference Reynolds number $Re = 2 \times 10^6$, based on the freestream conditions and a reference chord length, c, of 1 m, freestream turbulence intensity $Tu = 0.2$ % and turbulent viscosity coefficient ratio in the freestream $(\mu_t/\mu_\ell)_\infty = 10$.

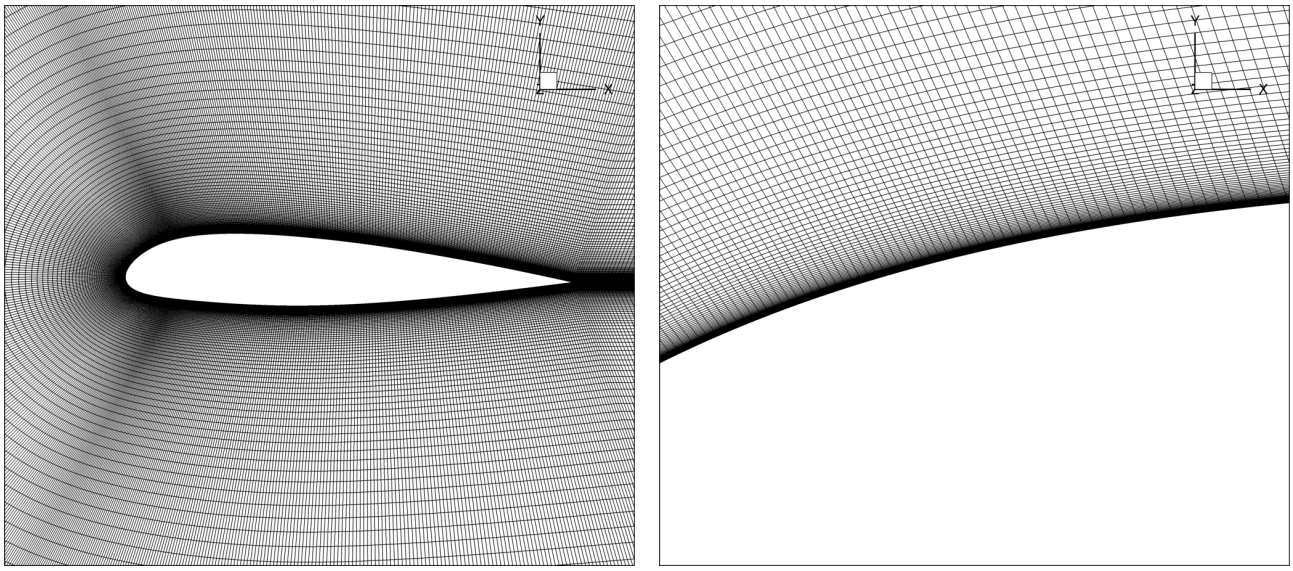

(a) Overview of the mesh used.

(b) Details of the mesh used.

Figure 1 – Computational mesh used for the *Aerospatiale-A* airfoil test case.

In the experimental documentation, it is highlighted that the experiments were carried out using 13.0 deg. of angle of attack. However, in order to compensate for wind-tunnel wall effects, in Ref. [20], the angle-of-attack value was re-defined as 13.3 deg. All the calculations performed in the present work, as well as those that led to the reference numerical results obtained in Refs. [2, 19], have used the corrected value of angle of attack of 13.3 deg. Figure 1 shows an overview of the mesh used for the studies here reported. This computational grid is composed of approximately 200,000 volumes and it follows the recommended guidelines for the use of eddy viscosity turbulence closures without wall modeling.

The pressure coefficient distributions obtained in the present calculations with the SST closure and with the SST model coupled to the $\gamma - Re_\theta$ transition model are compared to the experimental data in Fig. 2. As discussed, the present calculations have used the Green-Gauss theorem derivative calculation scheme for the viscous derivatives. The calculations with the SST closure alone seem to slightly underpredict the pressure coefficient values at the leading edge suction peak. On the other hand, the C_p distribution obtained with the $\gamma - Re_\theta$ transition model, together with the SST model, seems to present a better match with the experimental data. Another key difference can be seen at $x/c = 0.18$. At this point along the chord, the calculations with the transition model capture the separation bubble, while those with the SST closure alone completely ignore it. A different behavior is observed further downstream along the airfoil, at $x/c = 0.8$, where the experimental Cp distribution along the trailing edge separation region seems to be slightly better matched by the calculations using the SST closure alone.

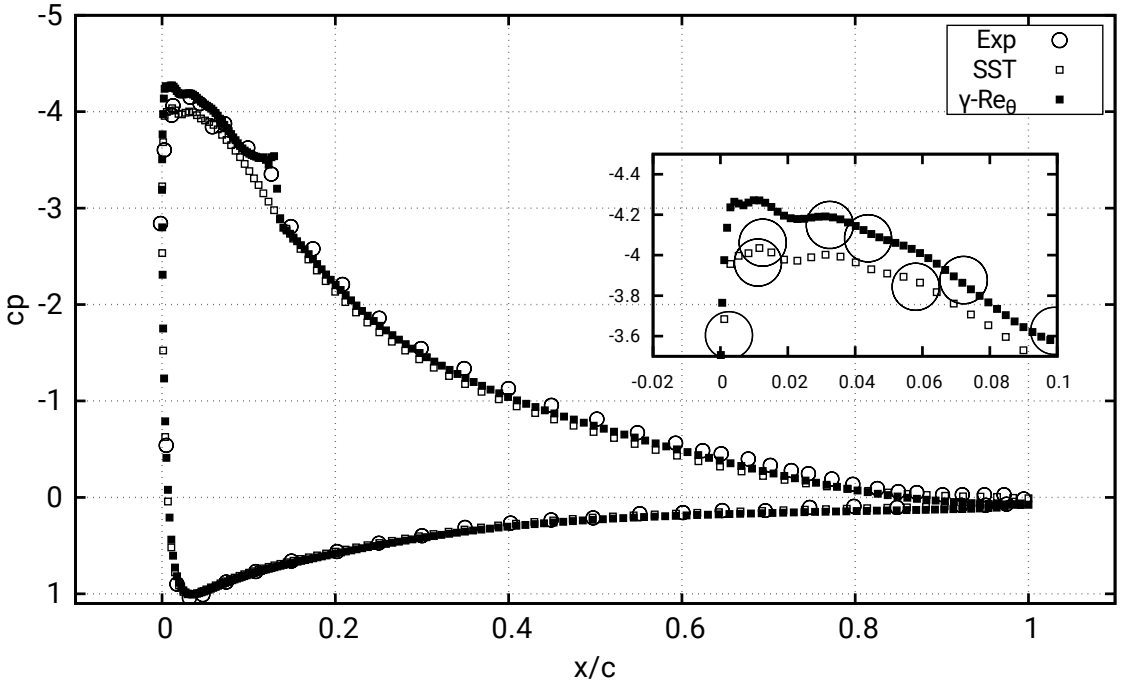

Figure 2 – Pressure coefficient distributions over the *Aerospatiale-A* airfoil at $M_\infty = 0.15$, $\alpha = 13.3$ deg. and $Re = 2 \times 10^6$.

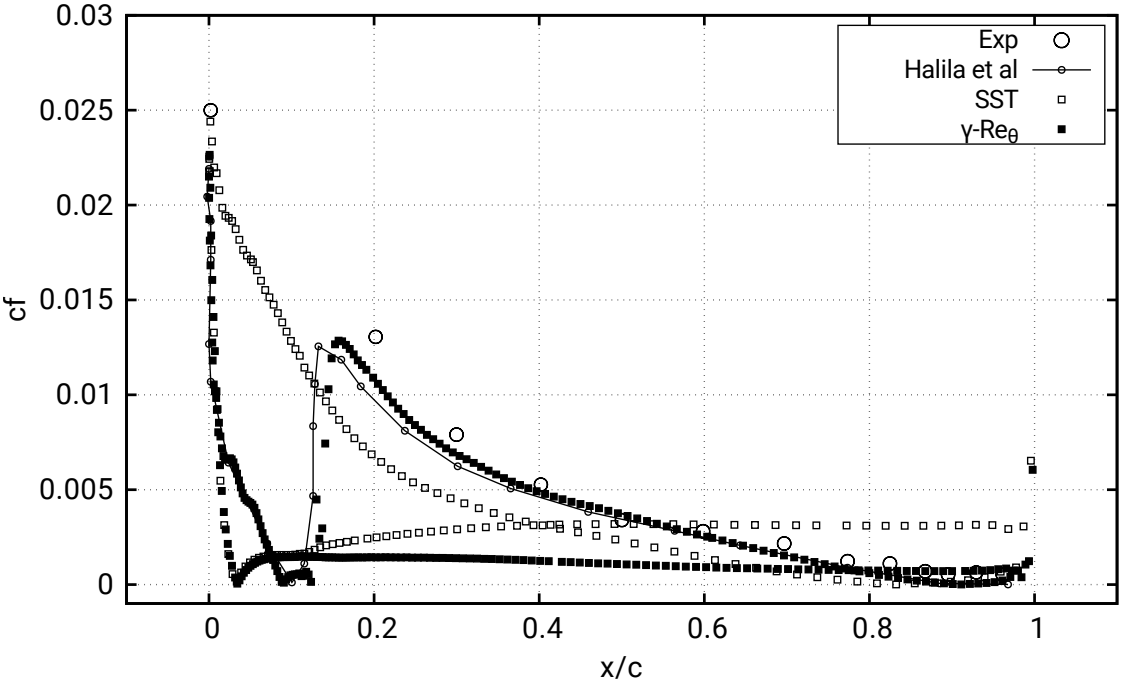

Figure 3 – Friction coefficient distributions over the *Aerospatiale-A* airfoil surface at $M_\infty = 0.15$, $\alpha = 13.3$ deg. and $Re = 2 \times 10^6$.

The friction coefficient distributions over the *Aerospatiale-A* airfoil surface, obtained with the SST model and with the $\gamma - Re_\theta$ transition model coupled to the SST closure, are compared to the experimental data and to the reference numerical results [2] in Fig. 3. The reference numerical results present a rapid increase in skin-friction coefficient at $x/c = 0.18$, over the airfoil upper surface, which is a clear indication of transition to turbulence. The present calculations with the $\gamma - Re_\theta$ transition model also have the same rapid increase in skin-friction coefficient, just slightly downstream along the airfoil. Actually, the present results, with the transition model, seem to provide a slightly better

match with the experimental data than those available in Ref. [2] at least up to $x/c = 0.4$. Downstream of that station, the C_f distribution obtained with the present code, with the transition model, is essentially indistinguishable from the one calculated in Ref. [2]. Clearly, the results obtained with the SST closure alone, also shown in Fig. 3, do not present any indication of the transition region. These results yield the C_f distribution typical of a fully turbulent simulation, with a very strong skin-friction coefficient peak at the leading edge. Airfoil upper surface C_f values, then, quickly decrease and are smaller than those obtained with the transition model calculations downstream of the transition point.

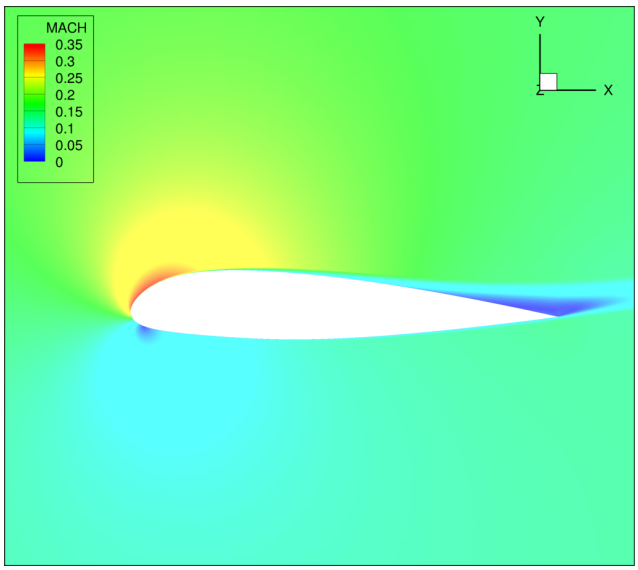

(a) Mach number contours, SST calculation.

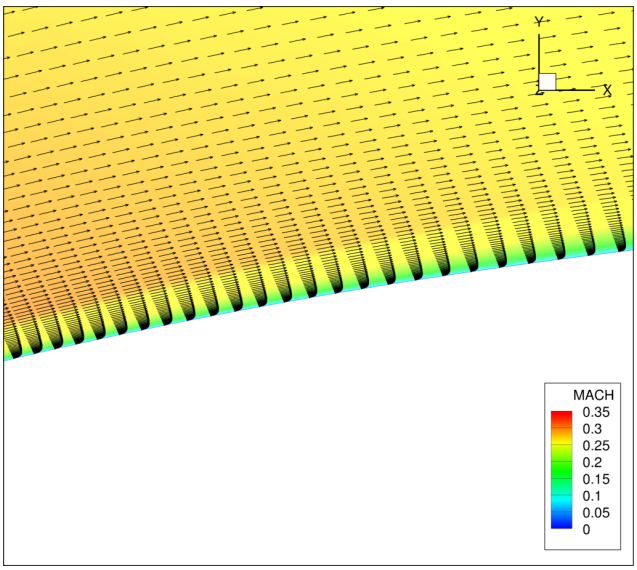

(b) Detail of the LSB region, SST calculation.

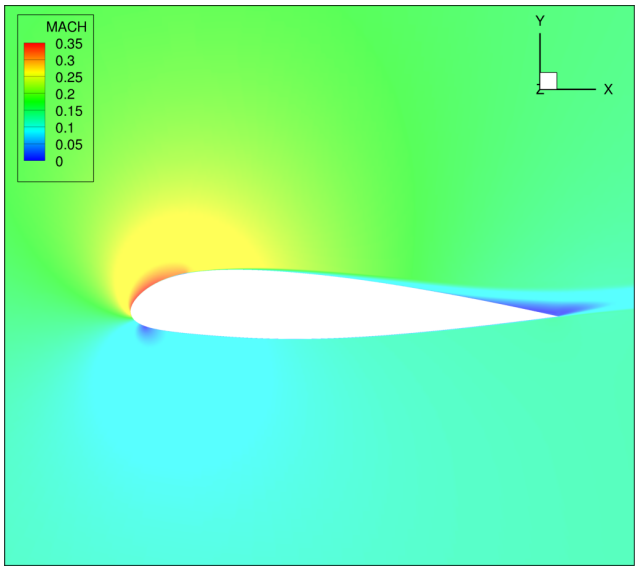

(c) Mach number contours, $\gamma - Re_\theta$ calculation.

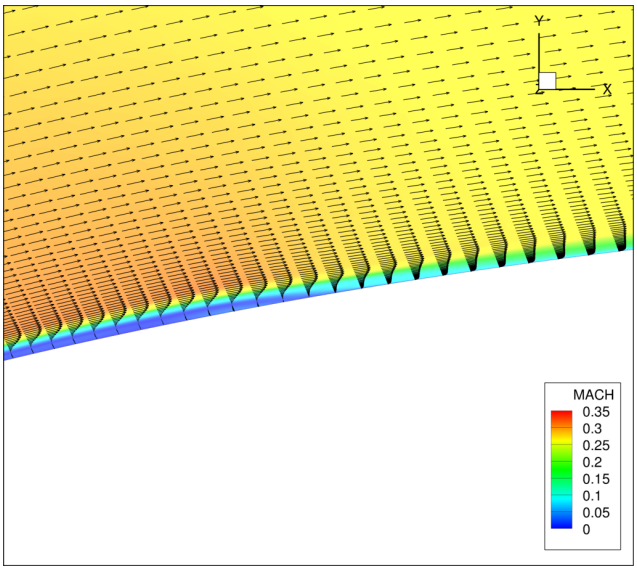

(d) Detail of the LSB region, $\gamma - Re_\theta$ calculation.

Figure 4 – Details of the laminar separation bubble over the *Aerospatiale-A* airfoil at $M_\infty = 0.15$, $\alpha = 13.3$ deg. and $Re = 2 \times 10^6$.

Mach number contours, superimposed by velocity vector profiles in order to help the visualization of the boundary layer behavior, are shown in Fig. 4, and they provide a good way of observing the solution in the laminar separation bubble region. Figures 4a and 4c show an overview of the Mach number contours over the airfoil. A classical high angle-of-attach flowfield is observed. The leading edge of the airfoil presents the highest values of Mach number while, at the trailing edge, a drastic reduction in Mach number values is observed. Figures 4b and 4d present a detailed view of the laminar separation bubble region. Velocity vector profiles are superimposed to the Mach number contours in order to further visualize the boundary layers. As already discussed, the calculations with the SST model alone do not present any separation, which is further emphasized by the boundary

layer profiles, which are standard turbulent velocity profiles. The results obtained with the $\gamma - Re_\theta$ transition model, shown in Fig. 4d, on the other hand, clearly indicate the presence of the laminar separation bubble. The figure also clearly shows the velocity profile inversions in the LSB and the turbulent reattachment of the shear layer downstream of the LSB.

The lift and drag coefficients for the *Aerospatiale-A* airfoil obtained with the SST closure and the $\gamma - Re_\theta$ transition model are organized in Table 1. This table presents the values of lift coefficient, c_ℓ, drag coefficient, c_d, and of viscous drag coefficient, c_{d_v}. The table also shows the variation in the calculated lift and drag coefficients with respect to the experimental data. One can see from the table that the lift coefficient values are accurately matched by both fully turbulent and transitional formulations. The lift coefficient result obtained with the transition model is even in much better agreement with the experimental data, as one might already expect from the pressure coefficient distributions shown in Fig. 2. On the other hand, the differences between experimental and numerical

Table 1 – Lift and drag coefficients obtained with the SST closure and the $\gamma - Re_\theta$ transition model.

Case	c_ℓ [-]	c_d [counts]	c_{d_v} [counts]	Δc_ℓ [%]	Δc_d [%]
Experiment	1.5620	208	N.A.	—	—
SST Model	1.4958	256	69.8	-4.4	$+23.0$
γ–Re_θ Model	1.5726	185	46.1	$+0.6$	-12.0

drag coefficients are much larger. One can see in Table 1 that the fully turbulent solution with the SST model is overpredicting the drag coefficient, with regard to the experimental value, whereas the calculation with the transition model is underpredicting it. Moreover, the difference between the two computational results is not entirely in the viscous portion of the drag, as one can also infer from the results in the table. In any event, the calculations with the transition model are still yielding results which are closer to the experimental data.

4.2 McDonnell Douglas 30P30N Multi-Element Airfoil

High-lift configurations are especially appealing test cases to apply transition modeling. The small reference length of flaps and slats, together with the relative lower aircraft speeds for take-off and landing, usually imply that these surfaces are subjected to low Reynolds numbers. As a consequence, laminar flow can be maintained over extensive portions of these devices. On the other hand, since laminar flows are more prone to separation when subjected to adverse pressure gradients, such conditions can trigger separated regions over the wing much earlier than when the flow is fully turbulent. Hence, laminar flow conditions may result in limitations to the operational envelope of the aircraft, although they would typically yield lower drag while the flow remains attached.

The configuration addressed in the present work is the McDonnell Douglas 30P30N Multi-Element Airfoil (MD 30P30N). The MD 30P30N airfoil is considered a standard 2-D high-lift test case that has a wide range of experimental data [21] available at different flowfield conditions. The condition that is under study here considers freestream Mach number $M_\infty = 0.2$, angle of attack $\alpha = 8$ deg., reference Reynolds number $Re = 9 \times 10^6$, based on the freestream conditions and a reference chord length, c, of 0.5588 m, freestream turbulence intensity $Tu = 0.8$ % and turbulent viscosity coefficient ratio in the freestream $(\mu_t/\mu_\ell)_\infty = 3$. This flight condition has also been numerically investigated in Refs. [4, 12], while the transition model was being developed, and by the present research group, while using a commercial CFD code, in Refs. [2, 19]. This test case is particularly interesting to address the bypass transition feature of the model due to the high values of turbulence intensity in the freestream. In this context, it is also a very good verification test case. Experimental skin-friction coefficient data over the MD 30P30N airfoil are available for this flight condition.

The computational mesh used in this case, shown in Fig. 5, is composed only by hexahedral cells. It must be emphasized that the in-house developed CFD code, used in the present study, only handles 3-D grids. Therefore, the simulation of a 2-D case is performed by extruding one computational cell in the third direction from the standard 2-D grid. The mesh used follows the recommended spacing in order to ensure y^+ values close to unit over all the airfoil components, as in the previous test case. The pressure coefficient distributions are shown in Fig. 6. In general, for the condition considered in

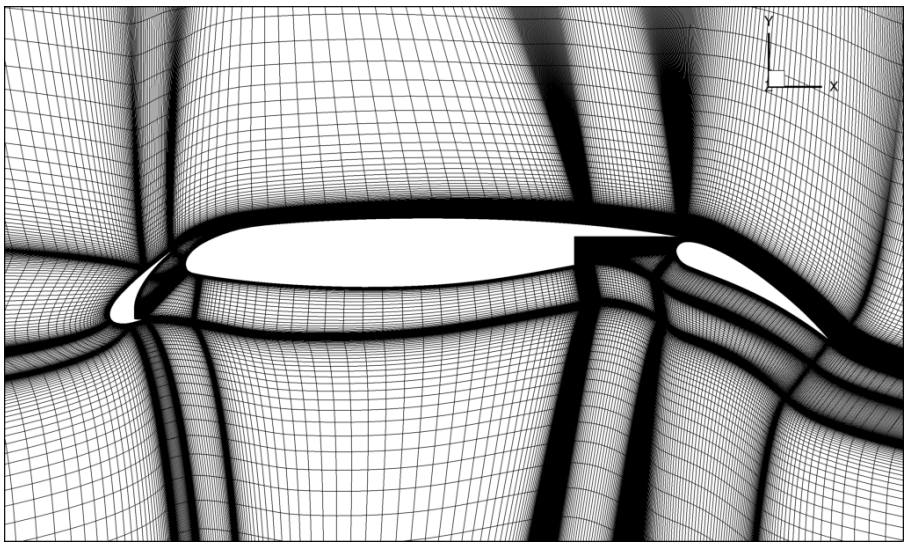

Figure 5 – Overview of the MD 30P30N multi-element airfoil computational mesh.

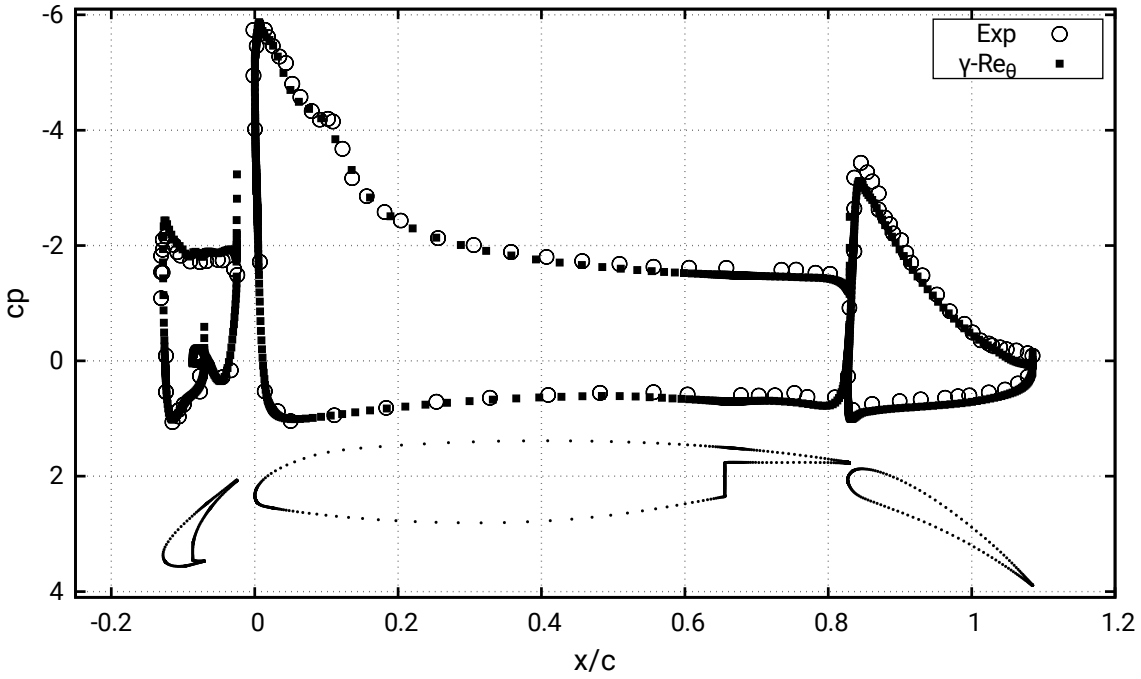

Figure 6 – Pressure coefficient distributions over the MD 30P30N multi-element airfoil at $M_\infty = 0.2$, $\alpha = 8$ deg. and $Re = 9 \times 10^6$.

the present work, a very good agreement is obtained between the pressure coefficient distribution calculated with the transition model and the experimental data. Somewhat larger discrepancies are seen at the suction peak in the flap element. It is interesting to observe that the Cp distributions at approximately 10% of the chord, on the upper surface of the main element, seem to have some non-smoothness in the pressure coefficient curves. This behavior is observed for both calculated and experimental data.

The distributions of friction coefficient over the MD 30P30N airfoil are shown in Fig. 7. The numerical results for the slat, the main element and the flap are presenting peaks of the skin-friction coefficient, which are typically associated with transition. The location of such peaks are indicative of bypass transition. The results in Fig. 7 also clearly indicate that the apparent kinks in the pressure coefficient distributions on the airfoil upper surface, at approximately 10% of the chord, observed in Fig. 6, for both computational and experimental data, are not associated with flow separation. Unfortunately, the distribution of experimental points over the slat or the main airfoil upper surface is rather sparse

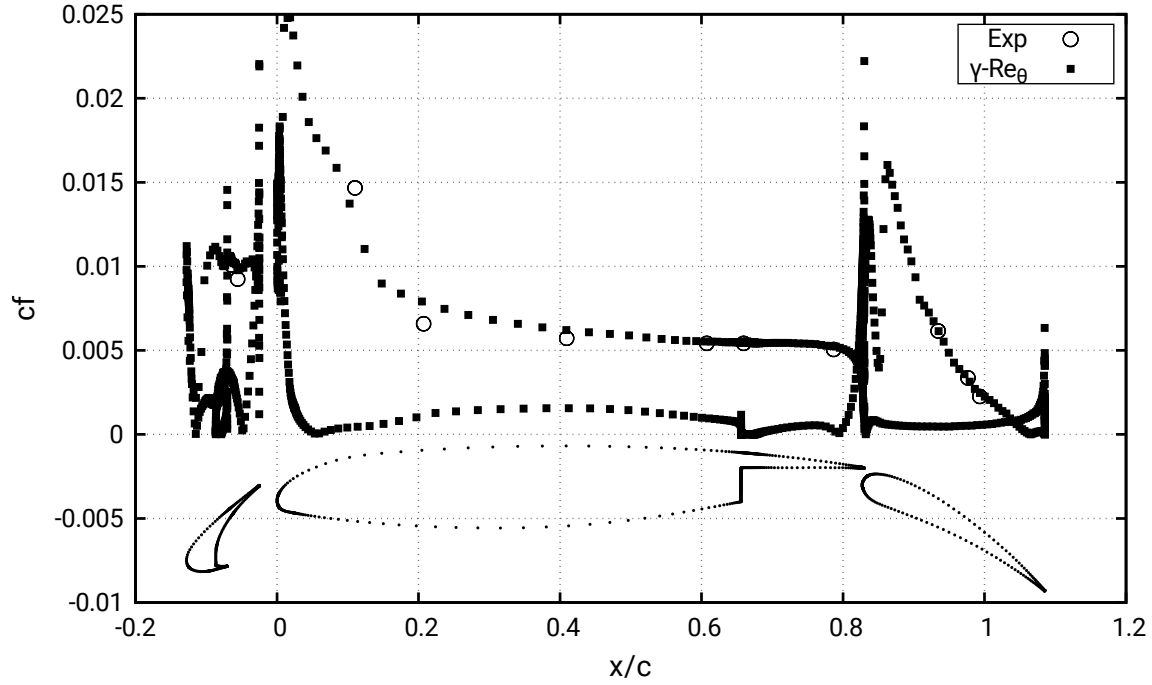

Figure 7 – Skin-friction coefficient distributions over the MD 30P30N multi-element airfoil at $M_\infty = 0.2$, $\alpha = 8$ deg. and $Re = 9 \times 10^6$.

and, in particular, there are no experimental data near the slat or the main airfoil leading edges. Therefore, it is difficult to directly assess the accuracy of the present computational results in the actual bypass transition regions. In any event, the comparison with the experimental data, where such data is available, for the C_f values over the main element and the flap component, is very good.

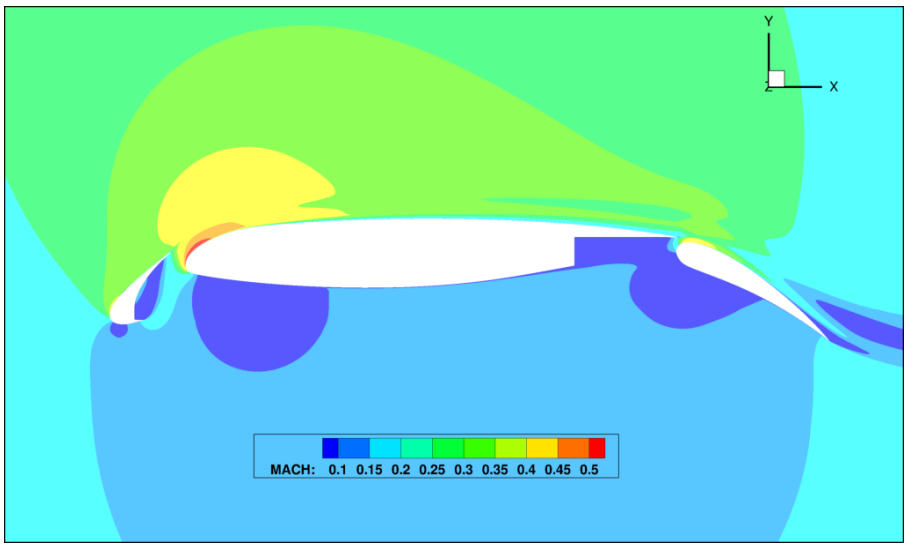

Figure 8 – Mach number contours for the flow over the MD 30P30N multi-element airfoil at $M_\infty = 0.2$, $\alpha = 8$ deg. and $Re = 9 \times 10^6$.

Figure 8 presents the Mach number contours for the flow over the MD 30P30N airfoil at the present flight condition. One can see that the slat component has an extensive recirculation bubble in the lower surface of the component, close to the main element. Moreover, the main airfoil element presents a region with strong acceleration in the upper surface, near the leading edge, as one would expect for the present high angle of attack case. However, no separation is seen over the main element. Finally, a small separation region can be observed in the upper surface near the flap trailing edge. All of these features are to be expected for the present configuration at this flight condition.

4.3 VLS Launch Vehicle

The last test case addressed in the present paper considers the supersonic flow over the VLS launch vehicle [22], which is a small satellite launcher which was developed in Brazil a few years back. The flow condition considers the freestream Mach number $M_\infty = 3.0$, zero angle of attack, reference Reynolds number $Re = 9 \times 10^6$, based on the freestream conditions and the diameter of the booster stage, freestream turbulence intensity $Tu = 0.5$ % and turbulent viscosity coefficient ratio in the freestream $(\mu_t/\mu_\ell)_\infty = 1$. This flight condition has been experimentally studied in Ref. [22] and numerically analyzed in Refs. [23, 24]. Previous attempts to compute the flow over the VLS configuration at this flight condition have only achieved some partial success.

In particular, the simulation results in the studies included in Refs. [23, 24] seem to suggest that the highly accelerated flow immediately downstream of the vehicle payload fairing could be prone to relaminarization. The vehicle has a boattail section downstream of the payload fairing, as indicated, for instance, in Fig. 9, and the experimental data indicate a fairly extensive flow separation region along the boattail for this flight condition. On the other hand, fully turbulent simulations in Refs. [23, 24] always predict an attached flow in the boattail region at this flight condition. Therefore, this is clearly a very interesting test case to be addressed with the use of a transition model. If, indeed, the separation region is only present when the boundary layer is laminar, the correct understanding of the physical phenomena occurring in this region of the vehicle could be very important in order to avoid problems involving the unsteady forces applied by separated flow over the vehicle.

Three levels of mesh refinement are considered in the present study. All meshes are composed solely by hexahedral cells, except at the upstream centerline where a face is collapsed into an edge. They are denoted here coarse, medium and fine meshes and they have, respectively, $894,432$, $2,304,960$ and $3,066,624$ cells. The grids have also been carefully crafted in order to guarantee y^+ values close to unit over the entire geometry. Figure 9 provides some visualizations of the various meshes. Both an overall view of the grid as well as a detailed visualization of the boattail region, for all three meshes, are shown in Fig. 9. It is clear from this figure that a fairly decent grid resolution is achieved in the region of interest for the present study. Moreover, one should observe that the present calculations are fully 3-D simulations, although only axisymmetric planes of the grids are shown in Fig. 9.

The Mach number contours for the flow over the VLS configuration at this flight condition are shown in Fig. 10. The visualization concentrates in the flow over the VLS forebody and, for the sake of clarity, the color scale has been amplified and positioned on the top of the image array. This figure has results for computations with the SST closure alone, in the medium mesh, and for the calculations with the $\gamma - Re_\theta$ transition model using all three mesh levels. It is clear from Fig. 10 that, aside from the behavior of the boundary layer in the boattail region, the results are very much alike for all calculations, as one should expect. The figure also clearly indicates that the calculations with the $\gamma - Re_\theta$ transition model, for all three grids, present a much thicker boundary layer along the boattail region and, in particular, at the compression corner at the end of the boattail than the results obtained with the SST model. This very thick boundary layer is already an indication that, probably, there is flow separation at the compression corner at the end of the boattail region. Actually, the results further indicate that, as the grid is refined, the computed boundary layer in the boattail gets thicker for the calculations with the transition model.

The details of the flow in the downstream portion of the boattail region are better visualized in Fig. 11. This figure presents Mach number contours superimposed by flow streamlines. The results shown in the figure are those calculated with the SST closure in the medium mesh and with the transition model in the fine grid. The profound differences between the separated region obtained with the SST closure calculation and the one resulting from the simulation with the $\gamma - Re_\theta$ transition model are clearly evident in Fig. 11. The results obtained with the fully turbulent simulation with the SST model show a very small reversed flow region at the compression corner in the downstream portion of the boattail section, as indicated in Fig. 11a. On the other hand, a quite extensive separated flow region is observed in Fig. 11b for the results from the calculation with the $\gamma - Re_\theta$ transition model. Essentially, most of the extension of the boattail is immersed in the reversed flow region.

The flow in the upstream portion of the boattail of the VLS launch vehicle can be considered equivalent to a flow over an expansion corner. The convex geometry implies that the boundary layer going

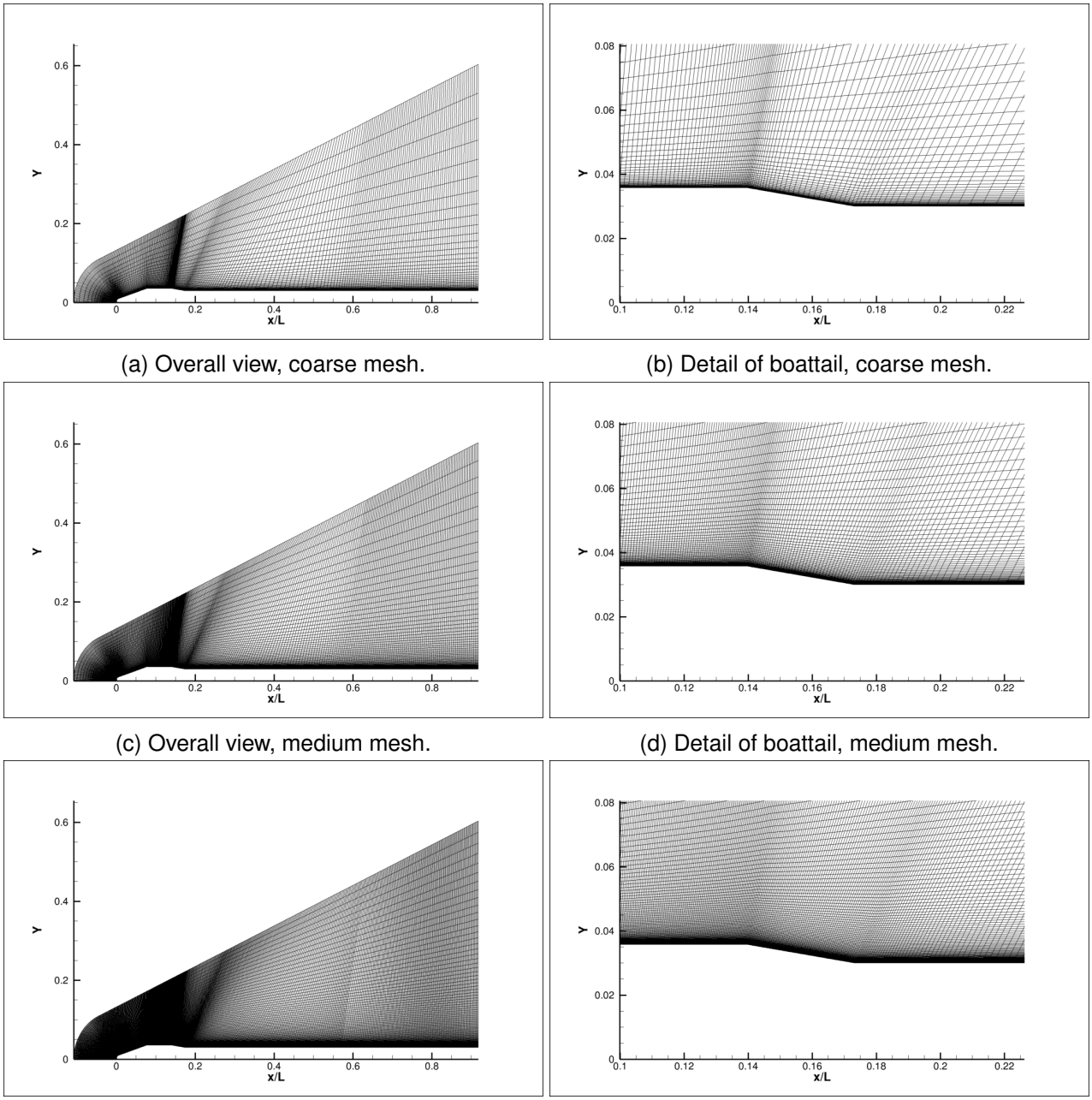

(a) Overall view, coarse mesh.

(b) Detail of boattail, coarse mesh.

(c) Overall view, medium mesh.

(d) Detail of boattail, medium mesh.

(e) Overall view, fine mesh.

(f) Detail of boattail, fine mesh.

Figure 9 – Computational meshes used for the flow simulations over the VLS configuration.

over the payload fairing-boattail junction is being subjected to a quite favorable pressure gradient. The opposite is true at the downstream end of the boattail, where the flow is essentially equivalent to that over a compression corner and it experiences a strong adverse pressure gradient. For the calculation with the SST model, this adverse pressure gradient is not strong enough to cause significant separation of the boundary layer. As the same pressure gradient seems to be sufficient to cause a fairly extensive separation in the results calculated using the transition model, the conclusion is that the turbulent state of the flow as it moves along the boattail must be quite different between the two calculations. This fact was the basis for the investigation of a possible flow relaminarization that was undertaken in the study reported in Ref. [23]. The hypothesis was that the rapid expansion going over the payload-booattail junction would create conditions for the occurrence of relaminarization. However, the calculations in Ref. [23], using some empirical correlations, do not support such hypothesis, as the state of the boundary layer in the upstream portion of the boattail is not sufficient to yield relaminarization.

Further insight into the flow behavior in the boattail region can be obtained by examining the pressure

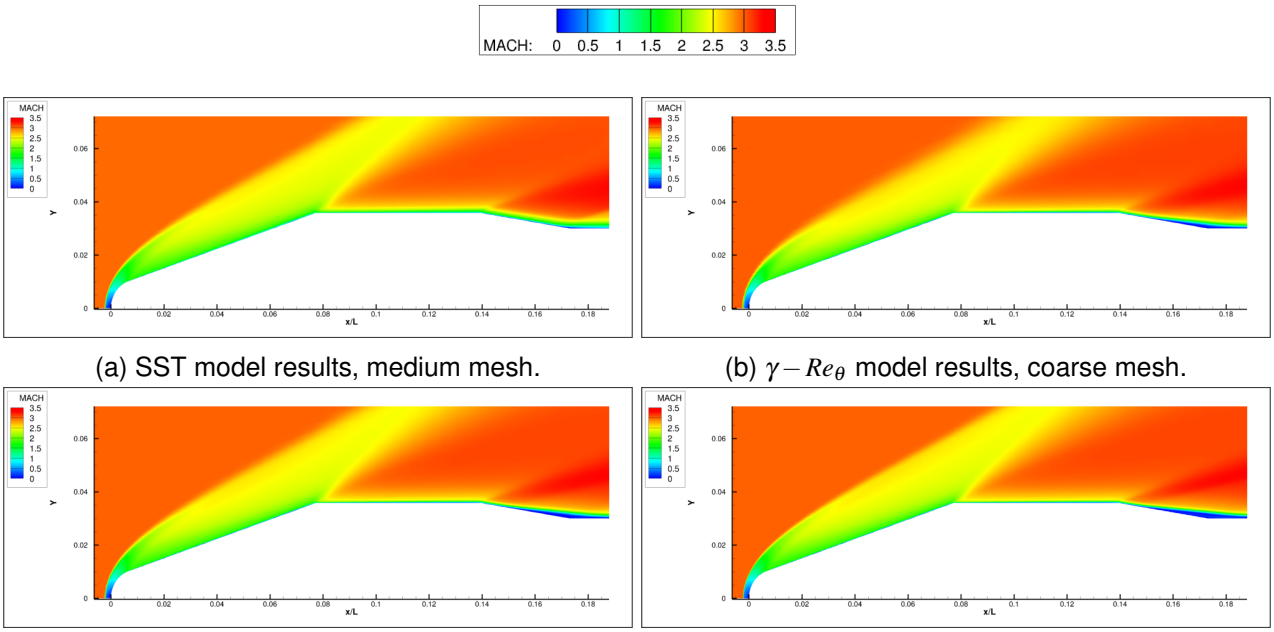

(a) SST model results, medium mesh.

(b) $\gamma - Re_\theta$ model results, coarse mesh.

(c) $\gamma - Re_\theta$ model results, medium mesh.

(d) $\gamma - Re_\theta$ model results, fine mesh.

Figure 10 – Mach number contours over the VLS launch vehicle forebody using different mesh refinements. Flight condition is $M_\infty = 3.0$, $\alpha = 0$ and $Re = 9 \times 10^6$.

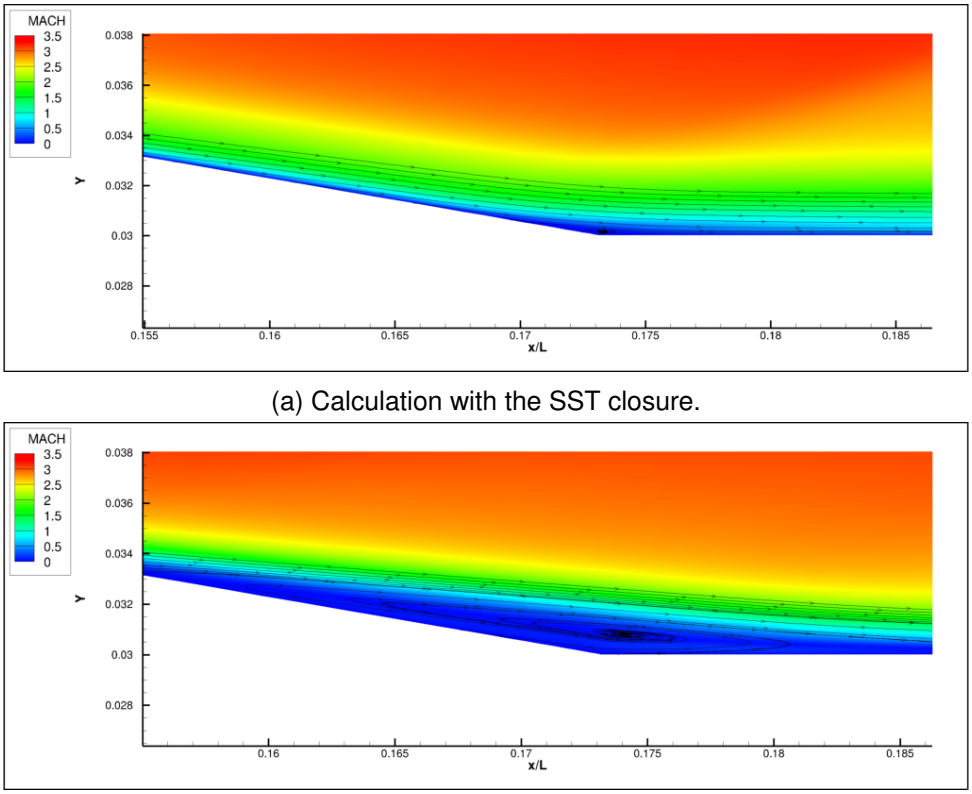

(a) Calculation with the SST closure.

(b) Calculation with the $\gamma - Re_\theta$ transition model.

Figure 11 – Mach number contours superimposed by flow streamlines in the boattail of the VLS launch vehicle. Flight condition is $M_\infty = 3.0$, $\alpha = 0$ and $Re = 9 \times 10^6$.

coefficient distributions along the VLS forebody. It is true that pressure does not convey information about turbulent quantities, but the issue in this case is flow separation and useful information on this behavior can be obtained by analyzing the pressure distribution. Figure 12 presents pressure coefficient distributions over the VLS forebody. Several curves are included in this figure, namely

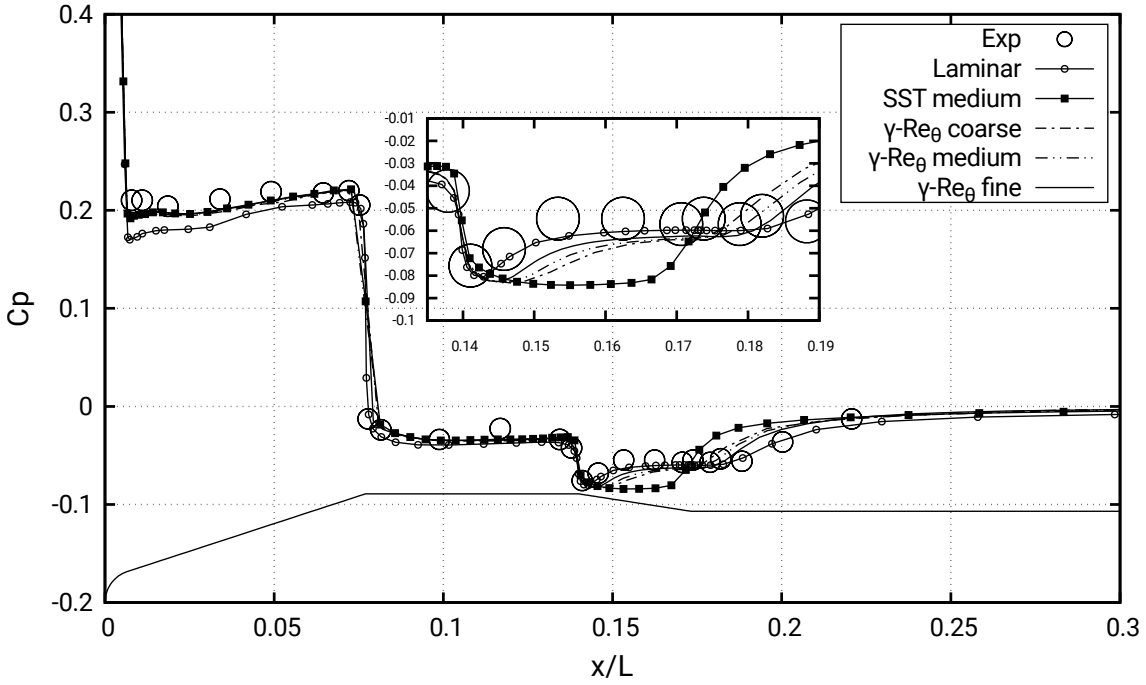

Figure 12 – Pressure coefficient distributions over the VLS launch vehicle. Flight condition is $M_\infty = 3.0$, $\alpha = 0$ and $Re = 9 \times 10^6$.

the results for the calculations with the SST model in the medium mesh, those for the calculations with the $\gamma - Re_\theta$ transition model with all three mesh levels here addressed, and the results for a simulation with the same CFD solver but without any turbulence modeling, calculated on the medium mesh. The latter are referred to in the figure as "laminar" results. All of these calculated pressure coefficient distributions are compared to the experimental data. Figure 12 also includes an inset with an enlarged view of the pressure coefficient distributions in the boattail region of the vehicle, which is very useful for the present discussion.

In general, the results in Fig. 12 are indicating that there is a very good agreement among the computed results and of those with the experimental data in the whole vehicle forebody, up to the beginning of the boattail region. One exception to this statement refers to the pressure coefficient distribution computed without any turbulence modeling at the conical portion of the vehicle nose. In this region, one can clearly observe that the calculations without any modeling yield C_p values which are considerably lower than the experimental data or those provided by the turbulent calculations. On the other hand, in the boattail region and downstream of there, the "laminar" results are precisely those that offer the best agreement with the experimental data. These results are indicating that, for the calculations without any modeling, the flow seems to be separating at essentially the same location as observed in the experiments. It is exactly the combination of these two observations that have led to the hypothesis of a possible relaminarization of the flow in past studies [23].

The interesting aspect that the present effort brings to the discussion is that the simulations with the transition model offer pressure coefficient distributions in the boattail region which are in between those obtained with fully turbulent calculations and those calculated without turbulence modeling. Moreover, the grid refinement study here performed indicates that, for the fine grid, the C_p distribution in the boattail is very close to that obtained with the "laminar" calculation. The fact that the simulations with the transition model are indicating a flow behavior quite similar to that of a "laminar" calculation is reinforced by the results in Fig. 13. This figure shows the friction coefficient distributions along the VLS forebody for all calculations here performed, *i.e.*, fully turbulent simulations with the SST model in the medium mesh, calculations with the transition model for all three mesh levels and simulations without any turbulence modeling in the medium mesh. One can clearly see in the figure that throughout the vehicle forebody, from very early in the conical nose and up to the end of the boattail, the C_f distributions obtained with the transition model are very similar to that obtained in the simulation

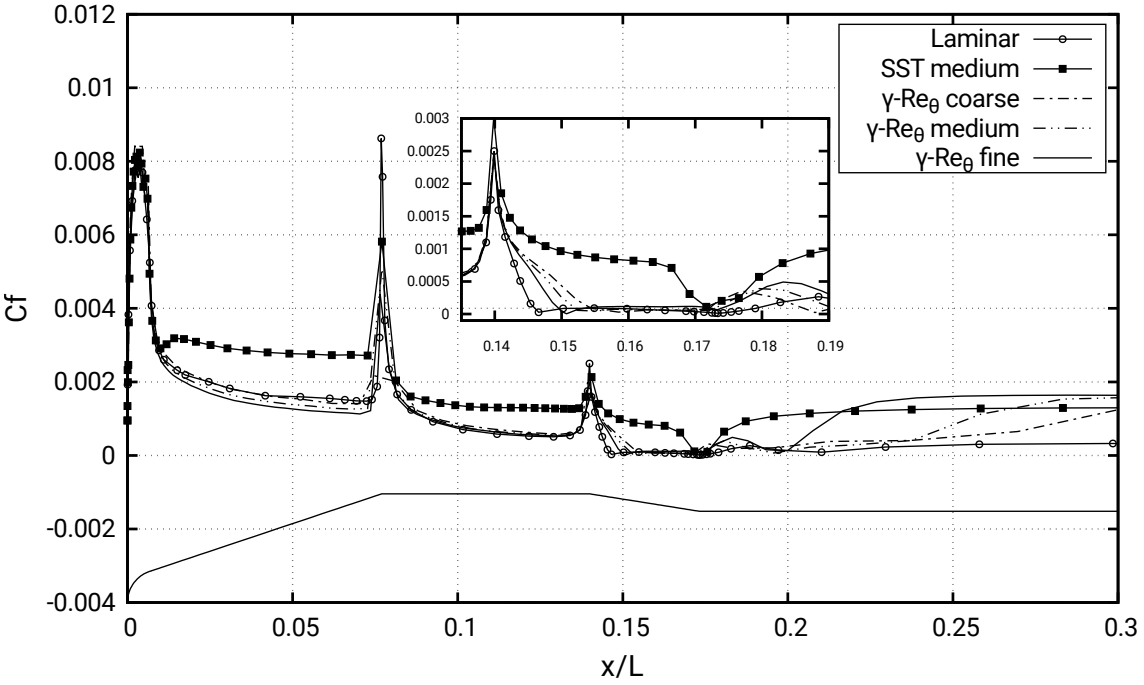

Figure 13 – Friction coefficient distributions over the VLS launch vehicle. Flight condition is $M_\infty = 3.0$, $\alpha = 0$ and $Re = 9 \times 10^6$.

without modeling. Moreover, the distribution yielded by the fully turbulent SST calculation is quite different from the other results. Figure 13 also has an inset with the details of the friction coefficient distributions in the boattail region and, as already pointed out, the results with the $\gamma - Re_\theta$ transition model in the fine grid are very similar to those obtained without modeling, at least up to the end of the boattail. The only significant difference is that the separation point is slightly downstream than the one predicted by the calculation without modeling.

5. Concluding Remarks

The present work has addressed the implementation and testing of a transition model into an existing in-house developed CFD solver. The test cases selected have included some classical high angle-of-attack airfoil configurations and a launch vehicle geometry. These test cases have experimental data available that could be used for verification and validation of the simulation capability developed. In general, the results obtained with the present simulation tool have shown very good correlation with the experimental data. In particular, the present results for the launch vehicle configuration have provided further understanding into the flow behavior at a supersonic flight condition for which all previous turbulent Reynolds-averaged Navier-Stokes computations have failed to yield the correct behavior at the vehicle boattail region.

Clearly, all the test cases addressed here deserve further studies. The space limitations in the paper have prevented us from discussing some aspects which should be the focus of additional analyses. For instance, the exact extension of the separated regions, in all three test cases, should be further investigated in order to understand the limitations of the present simulation capability. It is possible that additional grid refinement could improve the predictions of the transition model even further, especially considering the calculations for the launch vehicle configuration. Similarly, a detailed investigation of boundary layer profiles would be helpful in the understanding of more details of the flow over the two airfoil configurations, since this type of information is actually available from the experimental efforts for these test cases. Unfortunately, for the launch vehicle configuration, the experimental tests were mostly concerned with overall aerodynamic coefficients and, therefore, detailed pressure coefficient distributions is all that one can hope to obtain from the available experimental data. Nevertheless, the flow phenomena that seem to be occurring in the boattail region are very interesting for the present purposes of validating a transitional flow simulation capability.

6. Acknowledgments

The authors gratefully acknowledge the support for the present research provided by Conselho Nacional de Desenvolvimento Científico e Tecnológico, CNPq, under the Research Grant No. 309985/2013-7. The work is also supported by Fundação de Amparo à Pesquisa do Estado de São Paulo, FAPESP, under the Research Grant No. 2013/07375-0. The additional support provided by CNPq through a graduate scholarship for the first author is also greatly appreciated. The authors further acknowledge Dr. Marcello do Areal Souto Ferrari, who has graciously generated and provided the mesh for the MD-30P30N airfoil test case.

7. Contact Author Email Address

The authors of the present paper can be contacted at the following email addresses:
leonardo.mmoliva@gmail.com
ri_galdino@yahoo.com.br
joaoluiz.azevedo@gmail.com

8. Copyright Statement

References

[1] Langtry, R. B., *A Correlation-Based Transition Model using Local Variables for Unstructured Parallelized CFD Codes*, Ph.D. Thesis, University of Stuttgart, Stuttgard, Germany, 2006.

[2] Halila, G. L. O., Bigarella, E. D. V., and Azevedo, J. L. F., "Numerical Study on Transitional Flows Using a Correlation-Based Transition Model," *Journal of Aircraft*, Vol. 53, No. 4, Jul. 2016, pp. 922–941.

[3] Johnson, F. T., Tinoco, E. N., and Yu, N. J., "Thirty Years of Development and Application of CFD at Boeing Commercial Airplanes, Seattle," AIAA Paper No. 2003-3439*,16th AIAA Computational Fluid Dynamics Conference*, Orlando, FL, Jun. 2003.

[4] Menter, F. R., Langtry, R., and Volker, S., "Transition Modelling for General Purpose CFD Codes," *Flow, Turbulence and Combustion*, Vol. 77, Aug. 2006, pp. 277–303.

[5] Menter, F. R., "Two-Equation Eddy-Viscosity Turbulence Models for Engineering Applications," *AIAA Journal*, Vol. 32, No. 8, Aug. 1994, pp. 1598–1605.

[6] Bigarella, E. D. V. and Azevedo, J. L. F., "Advanced Eddy-Viscosity and Reynolds-Stress Turbulence Model Simulations of Aerospace Applications," *AIAA Journal*, Vol. 45, No. 10, Oct. 2007, pp. 2369–2390.

[7] Bigarella, E. D. V. and Azevedo, J. L. F., "A Unified Implicit CFD Approach for Turbulent-Flow Aerospace-Configuration Simulations," AIAA Paper No. 2009-1473*, 47th AIAA Aerospace Sciences Meeting Including The New Horizons Forum and Aerospace Exposition*, Orlando, FL, Jan. 2009.

[8] Mulas, M., Chibbaro, S., Delussu, G., Piazza, I. D., and Talisse, M., "Efficient Parallel Computations of Flows of Arbitrary Fluids For All Regimes of Reynolds," *International Journal of Numerical Methods for Heat & Fluid Flow*, Vol. 12, No. 6, 2002, pp. 637–657.

[9] Wilcox, D., "Dilatation Dissipation Corrections for Advanced Turbulence Models," *AIAA Journal*, Vol. 30, No. 11, Nov. 1992, pp. 2639–2646.

[10] Chien, K. Y., "Predictions of Channel and Boundary-Layer Flows with a Low-Reynolds-Number Turbulence Model," *AIAA Journal*, Vol. 20, No. 01, Jan. 1982, pp. 33–38.

[11] Menter, F. R., Kuntz, M., and Langtry, R. B., "Ten Years of Industrial Experience with the SST Turbulence Model," Turbulence, Heat and Mass Transfer 4: *Proceedings of the Fourth International Symposium on Turbulence, Heat and Mass Transfer*, Antalya, Turkey, Oct. 2003, pp. 625–632.

[12] Langtry, R. B. and Menter, F. R., "Correlation-Based Transition Modeling for Unstructured Parallelized Computational Fluid Dynamics Codes," *AIAA Journal*, Vol. 47, No. 12, Dec. 2009, pp. 2894–2906.

[13] Rumsey, C., "Turbulence Modeling Resource Web Page," `https://turbmodels.larc.nasa.gov/`, Last Access: 29-07-2020.

[14] Jameson, A. and Mavriplis, D., "Finite Volume Solution of the Two-Dimensional Euler Equations on a Regular Triangular Mesh," *AIAA Journal*, Vol. 24, No. 4, Apr. 1986, pp. 611–618.

[15] Roe, P. L., "Approximatte Riemann Solvers, Parameter Vectors, and Difference Schemes," *Journal of Computational Physics*, Vol. 43, No. 2, 1981, pp. 357–372.

[16] Cary, A. W., Dorgan, A. J., and Mani, M., "Towards Accurate Flow Predictions Using Unstructured Meshes," AIAA Paper No. 2009-3650*, 19th AIAA Computational Fluid Dynamics*, San Antonio, TX, Jun. 2009.

[17] Jalali, A., Sharbatdar, M., and Ollivier-Gooch, C., "Accuracy Analysis of Unstructured Finite Volume Discretization Schemes for Diffusive Fluxes," *Computers and Fluids*, Vol. 101, No. 2, Jun. 2014, pp. 220–231.

[18] Carvalho, L. M. M. O., Almeida, A. C. V. M., da Silva, R. G., Basso, E., and Azevedo, J. L. F., "Robust Parallel Computations of Turbulent Aerodynamic Flows," AIAA Paper No. 2018-1788*, 2018 AIAA Aerospace Sciences Meeting*, Kissimmee, FL, Jan. 2018.

[19] Halila, G. L. O., *A Numerical Study on Transitional Flows by Means of a Correlation-Based Transition Model*, M. Eng. Thesis, Instituto Tecnológico de Aeronáutica, São José dos Campos, SP, Brazil, 2014.

[20] Haase, W., Chaput, E., Elsholz, E., Leschziner, M., and Mueller, U. R., *ECARP–European Computational Aerodynamics Research Project: Validation of CFD Codes and Assessment of Turbulence Models*, Vol. 58 of *Notes on Numerical Fluid Mechanics*, Vieweg, Wiesbaden, Dec. 1997.

[21] Chin, V. D., Peters, D. W., Spaid, F. W., and McGhee, R. J., "Flowfield Measurements About a Multi-Element Airfoil at High Reynolds Numbers," AIAA Paper No. 1993-3137*, 24th Fluid Dynamics Conference*, Orlando, FL, Jul. 1993.

[22] Azevedo, J. L. F., Moraes Jr., P., Maliska, C. R., Marchi, C. H., and Silva, A. F. C., "Code Validation for High-Speed Flow Simulation Over Satellite Launch Vehicle," *Journal of Spacecraft and Rockets*, Vol. 33, No. 1, Jan.-Feb. 1996, pp. 15–21.

[23] Bigarella, E., *Advanced Turbulence Modeling for Complex Aerospace Applications*, Ph.D. Thesis, Instituto Tecnológico de Aeronáutica, São José dos Campos, SP, Brazil, 2007.

[24] Bigarella, E. D. V. and Azevedo, J. L. F., "Numerical Study of Turbulent Flows over Launch Vehicle Configurations," *Journal of Spacecraft and Rockets*, Vol. 45, No. 2, Mar. 2005, pp. 266–276.